Supplement of Atmos. Chem. Phys., 26, 5313–5332, 2026
https://doi.org/10.5194/acp-26-5313-2026-supplement

Atmospheric Chemistry and Physics
Open Access
EGU

Supplement of

Impacts of summertime photochemical aging on the physicochemical properties of aerosols in a Paris suburban forest region

Chenjie Yu et al.

Correspondence to: Chenjie Yu (chenjie.yu@lisa.ipsl.fr) and Vincent Michoud (vincent.michoud@lisa.ipsl.fr)

S1 Air mass history examples from UK NAME dispersion model

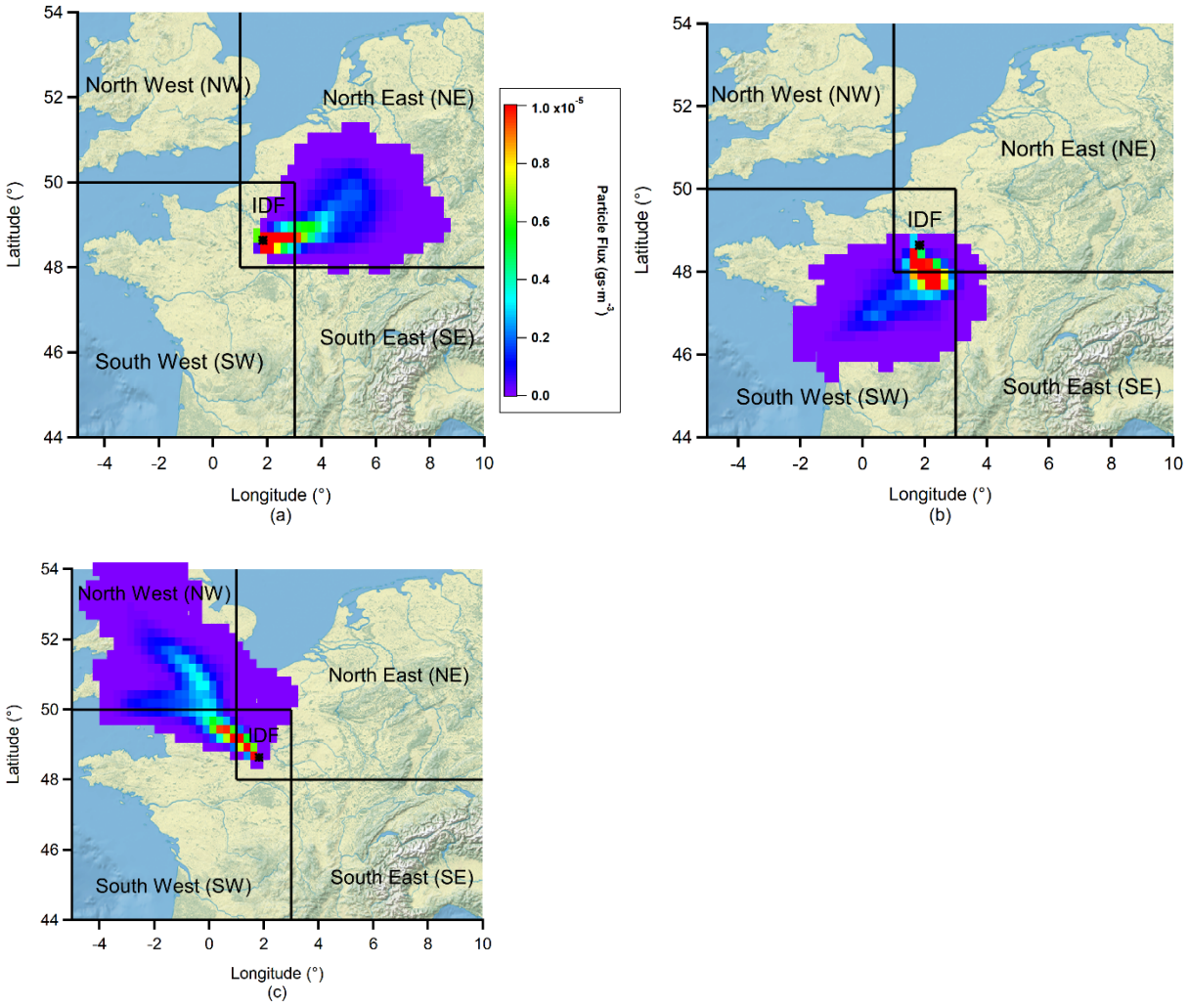

Figure S1: Examples of different external air mass sources dominated periods: (a) Northeast (NE) airmass-dominated period (12:00 UTC 11/07/2022); (b) Southwest (SW) airmass-dominated period (12:00 UTC 01/07/2022); and (c) Northwest (NW) airmass-dominated period (12:00 UTC 05/07/2022).

S2 Spatial distribution of fire points

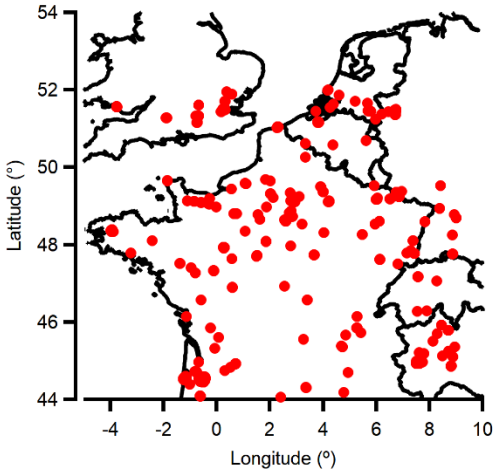

Figure S2: Spatial distribution of fire points during the ACROSS project period observed by MODIS.

S3 HR-AMS Ionization Efficiency (IE) and Relative Ionization Efficiency (RIE) factors and detection limit

IE	3.00E-07	
	RIE	Detection limit of HR-AMS V-mode (μg/m³)
OA	1.4	0.069
SO4	0.88	0.022
NO3	1.1	0.016
NH4	4	0.070
Chl	1.3	0.022

Table S1: Ionization Efficiency (IE) and Relative Ionization Efficiency (RIE) applied for HR-AMS data analysis. Detection limits for NR-PM_1 species were calculated as three times the standard deviation (3σ) of mass concentrations measured during filter periods, following the approach of Decarlo et al. (2006). The HR-AMS data were recorded at a ~3 min time resolution.

S4 Positive Matrix Factory analysis from HR-AMS

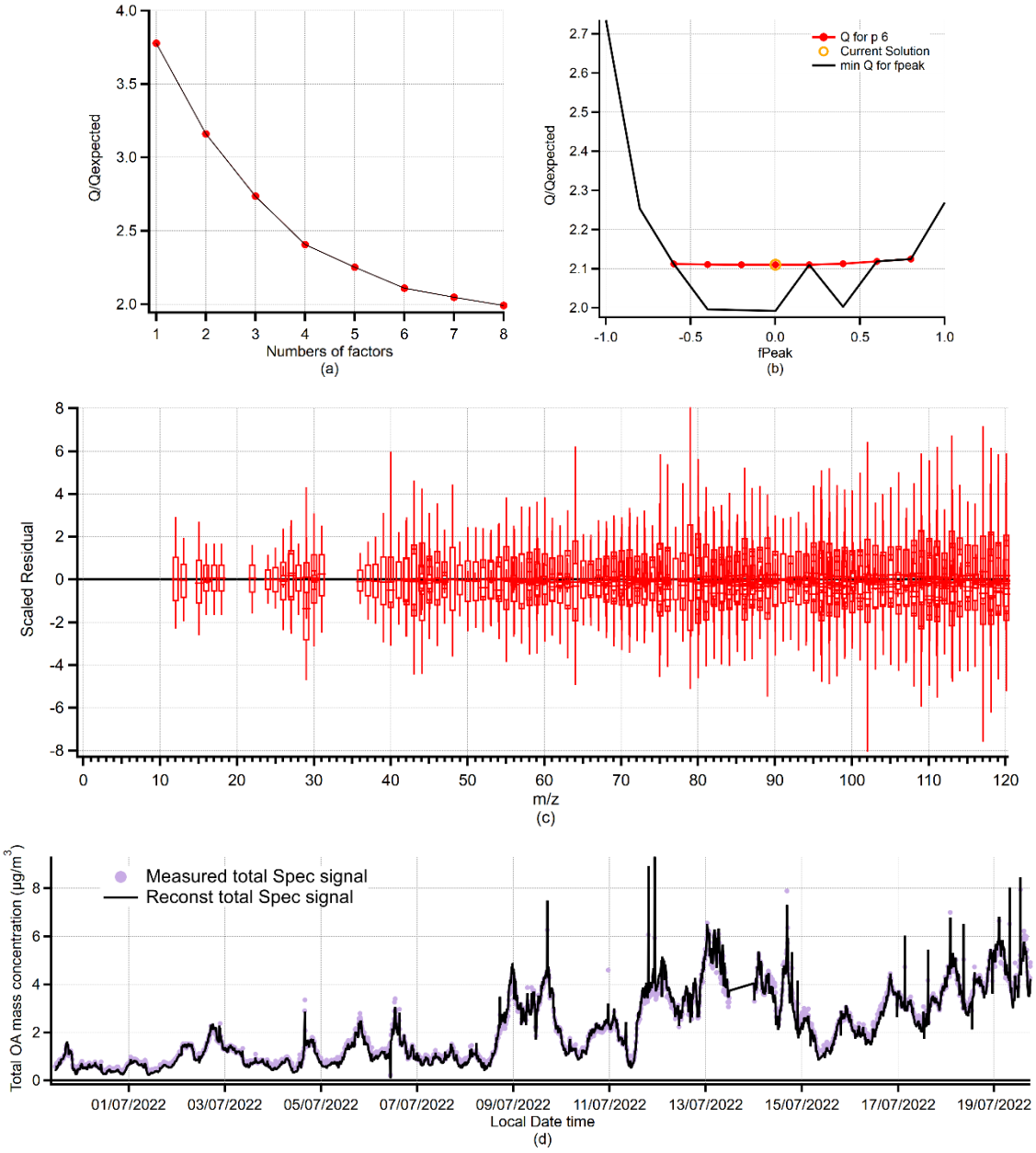

Figure S3: PMF diagnostic plots: (a) Quality-of-fit parameter $Q/Q_{expected}$ varied as a function of the number of factors, (b) $Q/Q_{expected}$ varied as a function of fpeak, (c) scaled residual for each m/z, (d) time series of measured and PMF reconstructed OA mass concentrations.

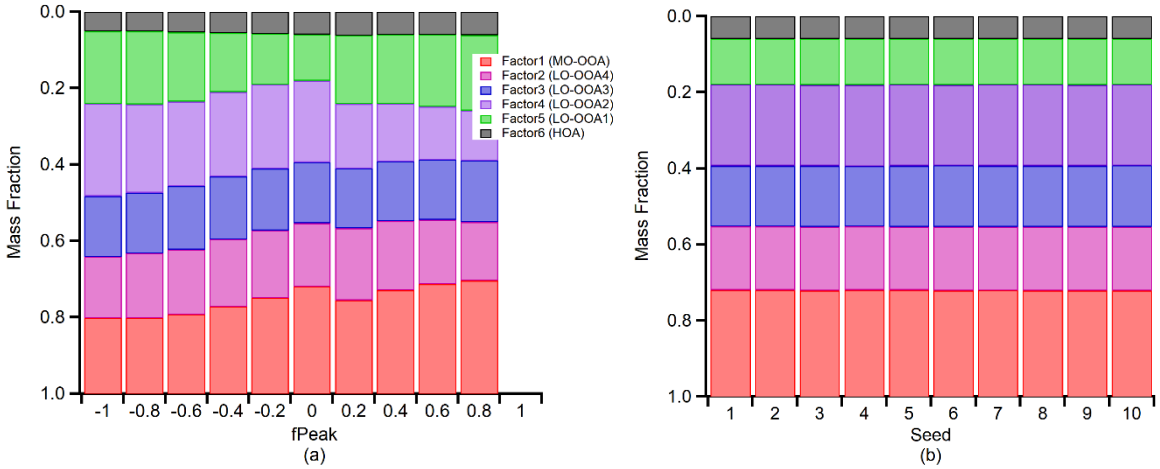

Figure S4: Mass fraction of PMF factors for six-factor solution as a function of (a) fPeak, (b) Seed.

30

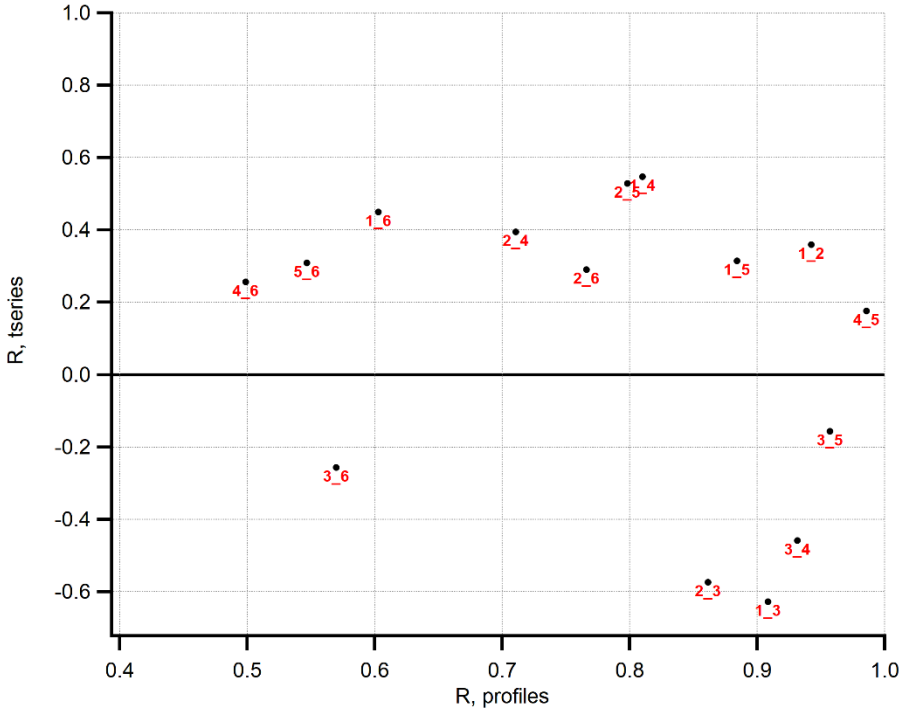

Figure S5: Correlations of the time series and spectral profiles among the PMF factors. The factor numbers refer to: (1) MO-OOA; (2) LO-OOA4; (3) LO-OOA3; (4) LO-OOA2; (5) LO-OOA1; (6) HOA

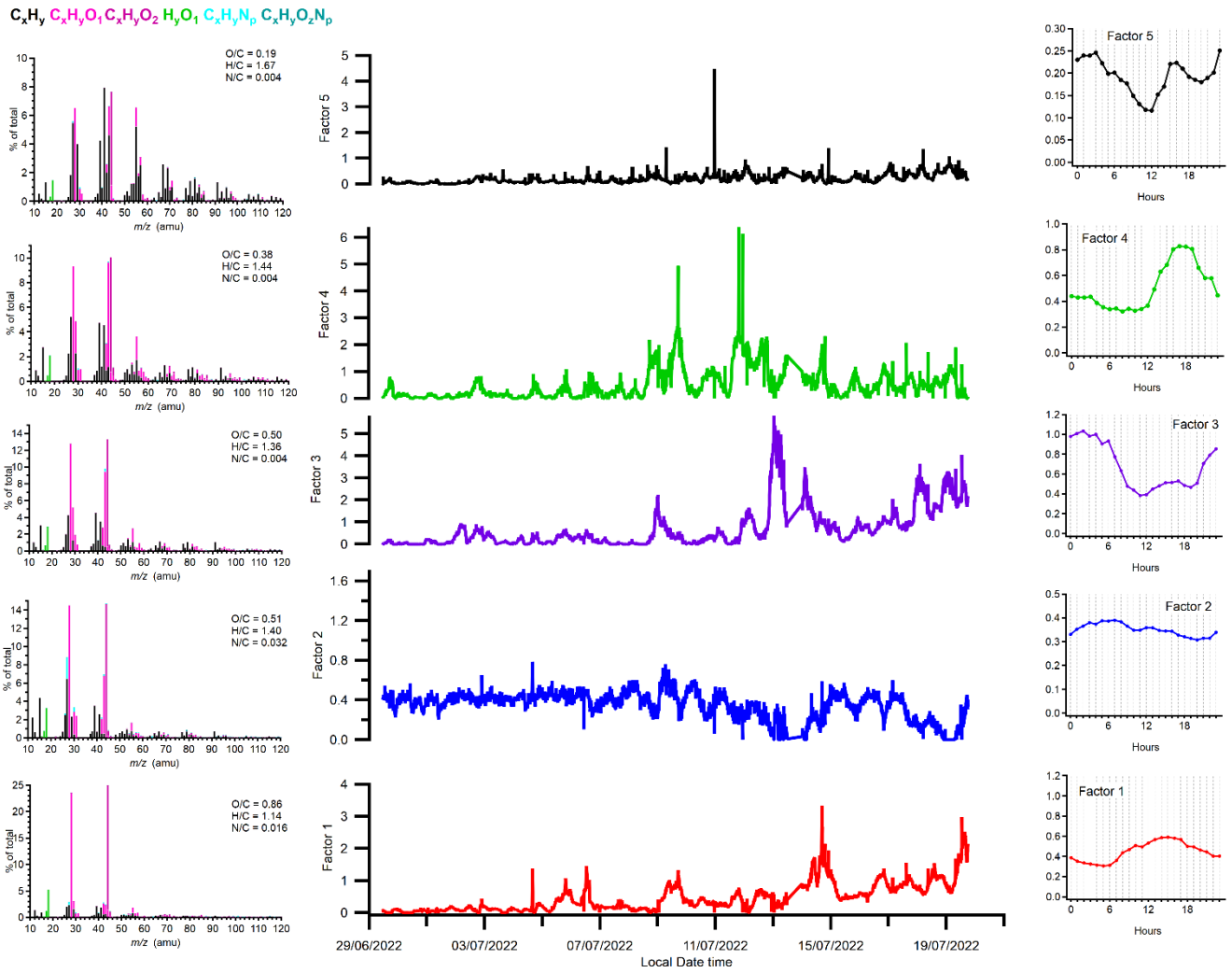

Figure S6: The average mass spectra and time series for 5-factor solution. Factor 4 is a mixed factor of LO-OOA1 and LO-OOA4. The HOA factor is not distinctly resolved in the 5-factor solution because Factor 5 represents a mixture of HOA and secondary compounds. This is evidenced by its afternoon concentration peak which is similar to the other OOA factors.

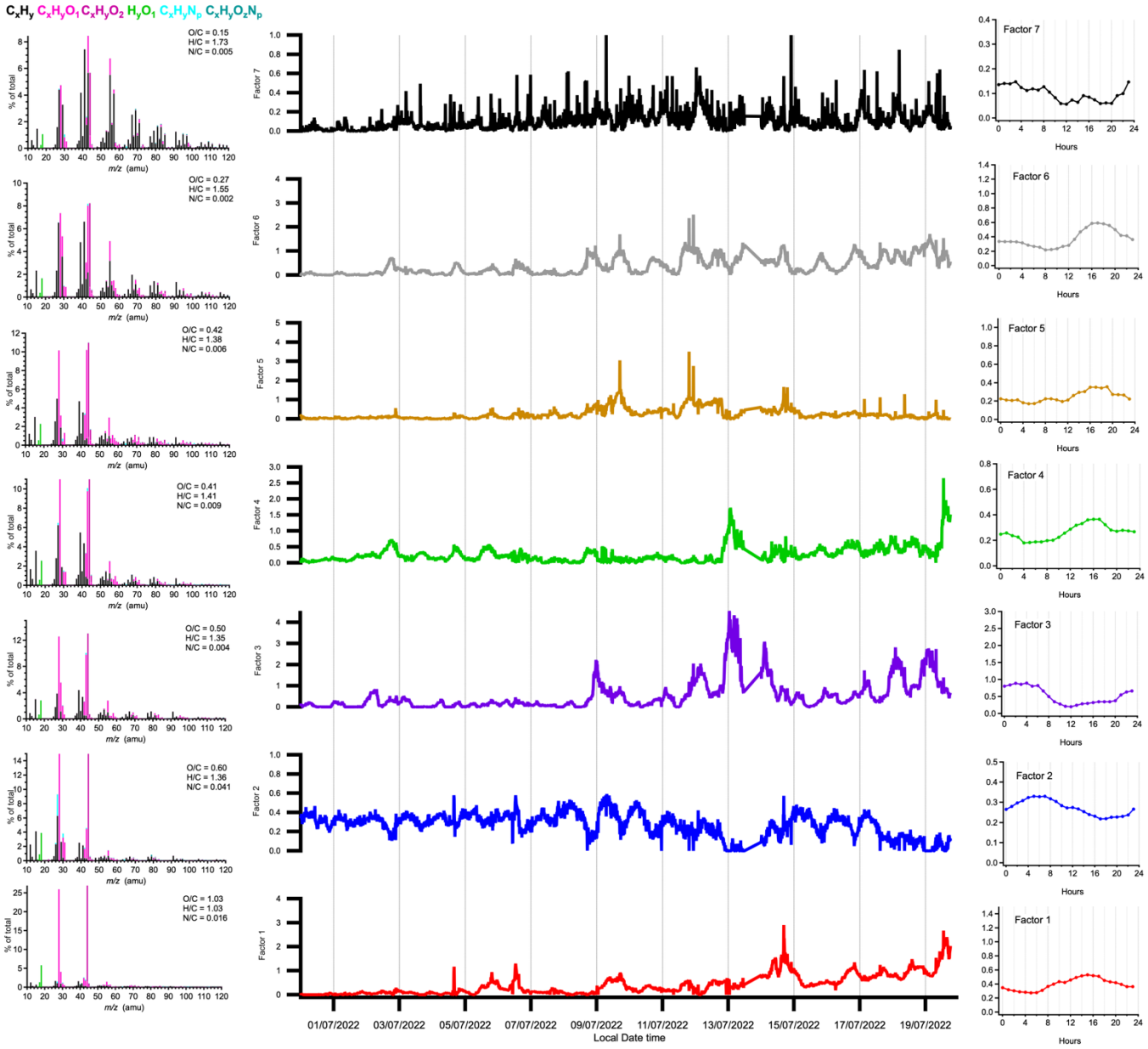

Figure S7: The average mass spectra and time series for 7-factor solution. The LO-OOA1 splits into two factors (Factor 3 and Factor 5). The 7-factor solution exhibited greater rotational ambiguity, as indicated by significant variation in factor mass fractions across the fPeak range (-1 to 1).

45

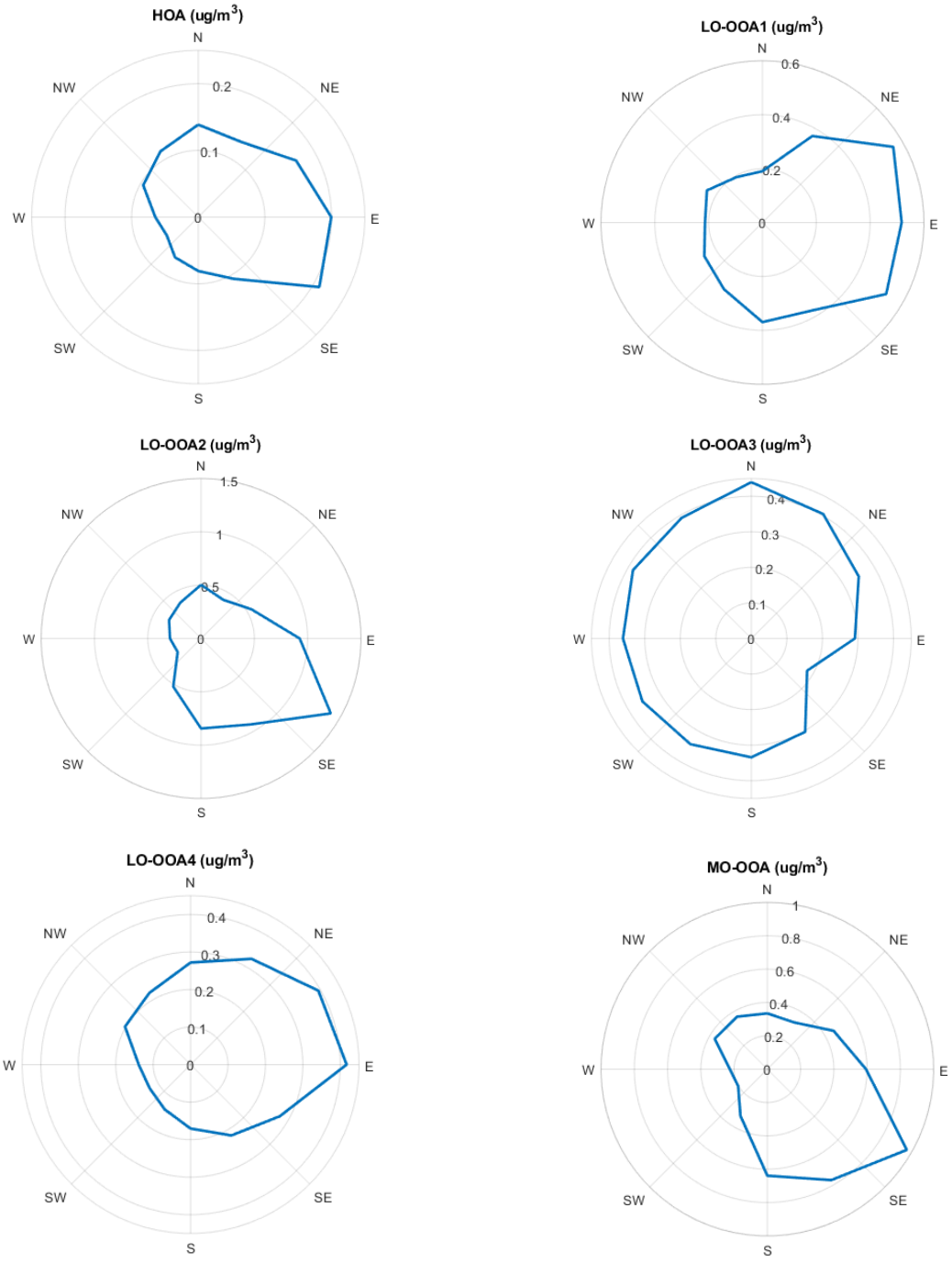

Figure S8: Wind rose for the PMF factors.

S5 Comparison of HR-AMS PMF factor mass spectra with previous studies

Table S2 presented cosine similarity between the AMS PMF factor mass spectra derived in this study and those from Crippa et al. (2013). Cosine similarity of the AMS PMF factor mass spectra is calculated following the methods described in Jeon et al. (2023). The HOA factor resolved here shows a strong similarity (cosine similarity > 0.9) with the primary OA identified in previous measurements. In Crippa et al. (2013), OOA was further classified by volatility, with LV-OOA exhibiting a higher oxidation state than SV-OOA. This classification is consistent with our results: LO-OOA1 and LO-OOA2, characterized by lower O:C ratios, closely resemble the spectra of SV-OOA, whereas LO-OOA3, LO-OOA4, and MO-OOA show stronger similarity with the spectra of LV-OOA.

AMS PMF factors in this study	AMS PMF factors from previous Paris 2009 summer study (Crippa et al., 2013)				
	Cooking OA (COA)	HOA	Semi Volatility (SV)-OOA	Marine OA (MOA)	Low Volatility (LV)-OOA
HOA	**0.91**	**0.92**	0.86	0.76	0.73
LO-OOA1	0.75	0.82	**0.94**	0.86	0.88
LO-OOA2	0.62	0.76	**0.94**	0.88	**0.94**
LO-OOA3	0.41	0.55	0.74	0.76	**0.96**
LO-OOA4	0.38	0.53	0.70	0.76	**0.98**
MO-OOA	0.26	0.39	0.57	0.67	**0.94**

Table S2 Cosine similarity between the AMS PMF factor mass spectra derived in this study and those from previous summer measurements in urban Paris (Crippa et al., 2013). Cosine similarity values greater than 0.9 are highlighted in bold and considered similar

S6 HR-AMS above- and below canopy comparison

Figure S9 and S10 show the time series of below- and above-canopy NR-PM_1 and diurnal differences in PMF results during the ACROSS project, respectively. Throughout the campaign, differences in NR-PM_1 between the two heights were only observed at night till the early dawn the next day. This was likely attributed to airmasses above- and below-canopy decoupling and near-ground formation of LO-OOA2 from local vegetation at night. After sunrise (~06:00), the boundary layer height increased, enhancing vertical mixing and reducing surface-level concentration contrasts. Consequently, the above- and below-canopy differences became less pronounced during the daytime under well-mixed conditions.

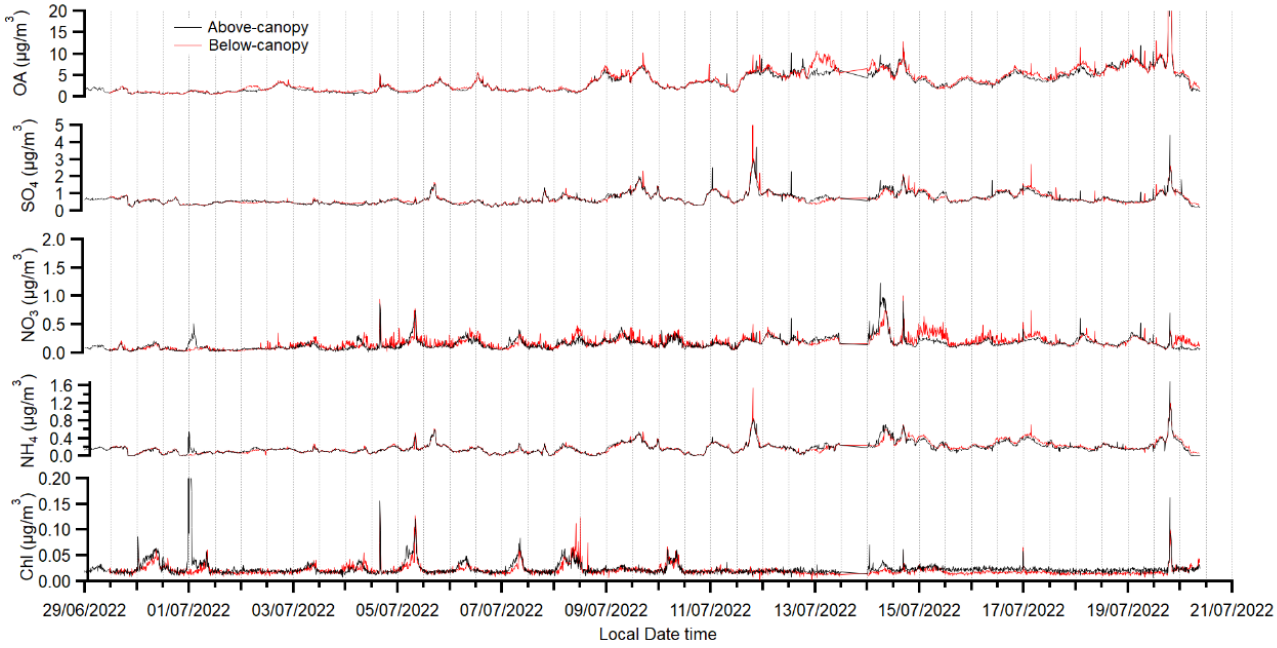

Figure S9 Time series of HR-AMS NR-PM_1 results below- and above- canopy

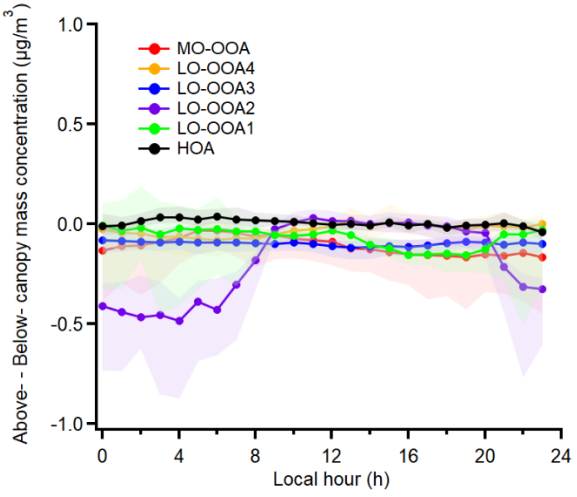

Figure S10: Diurnal differences in HR-AMS OA PMF factor mass concentrations above and below the canopy. The lower and upper whiskers in the figure are the 25th and 75th percentiles, respectively.

S7 Evolution of gas phase compounds due to photochemical aging

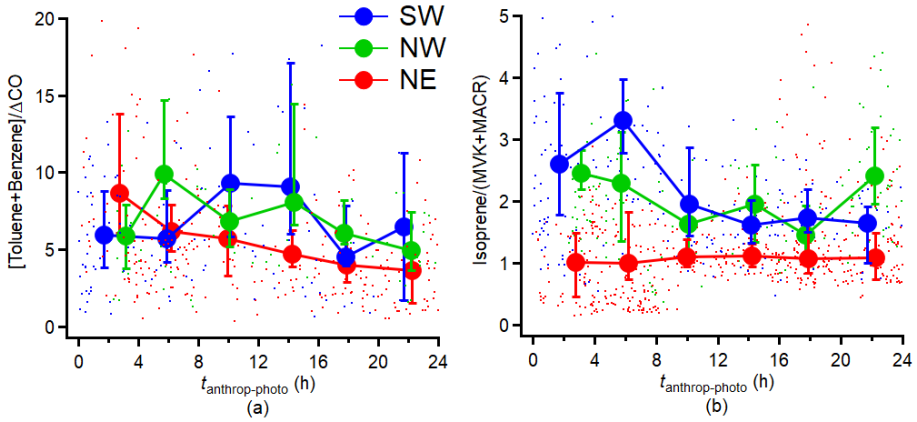

Figure S11: Variations in (a) Sum of Toluene and Benzene normalised to CO concentration; (h) ratio between isoprene and MVK+MACR as a function of $t_{anthrop-photo}$. The results are averaged into four-hour intervals along $t_{anthrop-photo}$ and the error bar indicates the 25th and 75th percentiles, respectively.

Figure S11 presents the evolution of (a) sum of normalised toluene and benzene concentration. (b) ratio between isoprene and MVK+MACR as a function of $t_{anthrop-photo}$ The background CO was defined as the 5th percentile of the entire campaign period (with BB influenced period removed) and was estimated to be 52 ppb. A decreasing trend was observed for the primary anthropogenic VOCs (Toluene + Benzene) during the NE period. However, the (Toluene + Benzene)/ΔCO concentrations remained independent of $t_{anthrop-photo}$ for the other periods. This was likely attributable to either instrumental interference, as a fraction of monoterpenes is known to fragment under PTR-MS ionization conditions, producing ions at m/z 93 (Tani et al., 2003; Ambrose et al., 2010), or to biogenic emissions of toluene from certain plant species (Misztal et al., 2015; White et al., 2009). During the NE air mass dominated period, pollution levels were higher, resulting in higher anthropogenic emitted toluene concentrations. Under these polluted conditions, the relative interference from biogenic emissions became less significant, and the decreasing trend of (Toluene + Benzene)/ΔCO was more clearly observed compared to other periods.

As shown in Figure S11(b), the ratio of isoprene to MVK+MACR decreased during the SW period, while its variation was limited during the NE period. This was likely due to both enhanced daytime isoprene emissions and more active photochemical process of MVK+MACR under the strong solar radiation and high temperatures characteristic of the NE period.

S9 Multiple linear regression (MLR) between $\sigma_{\text{abs BrC,470}}$ and all PMF-derived factors

$\sigma_{\text{abs BrC,470}}$ (R^2 = 0.54)		
HR-AMS PMF factor	Regression coefficient a_i	Partial correlation coefficient (multivariate)
HOA	0.49	0.22
LO-OOA1	-0.06	-0.06
LO-OOA2	0.03	0.07
LO-OOA3	0.49	0.18
LO-OOA4	0.34	0.29
MO-OOA	0.40	0.58
Intercept		-0.08

Table S4 Results of multiple linear regression (MLR) between $\sigma_{\text{abs BrC,470}}$ and individual PMF-derived factors, all the PMF-derived factors are included here.

S10 Evaluation of NO_x/NO_y-derived relative anthropogenic photochemical age

To validate whether NO_x/NO_y-derived $t_{\text{anthrop-photo}}$ provides a robust representation of the relative aging of transported air masses, a trajectory-based transport age was derived as an independent validation. The trajectory-based transport age is defined as the time elapsed between the observation time at the measurement site and the first intersection of the backward trajectory with the corresponding anthropogenic emission region. The trajectory-based transport age was calculated from hourly NAME model outputs.

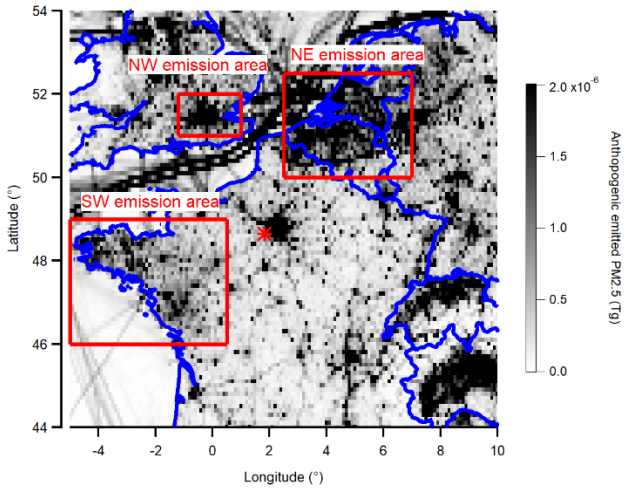

Figure S12. Spatial distribution of anthropogenic $PM_{2.5}$ emissions from the EDGAR inventory, averaged over June–July 2022. Three anthropogenic emission regions were identified based on high-emission hotspots.

As presented in Figure S12, three dominant anthropogenic emission area was identified through the EDGAR anthropogenic $PM_{2.5}$ emission inventory (0.01° × 0.01° resolution) during the campaign period: (1) NE emission region, (50° – 52.5° N, 2.5° – 7° E); (2) NW emission region (51° – 52°N, -1.2° – 1°E); (3) SW region (46° – 49° N, -5° – 0.5° E). As shown in Figure 2, the SE air mass influenced the site only for a few hours during the afternoon of 19 July. Therefore, emissions from the Po Valley in the SE region were not considered here.

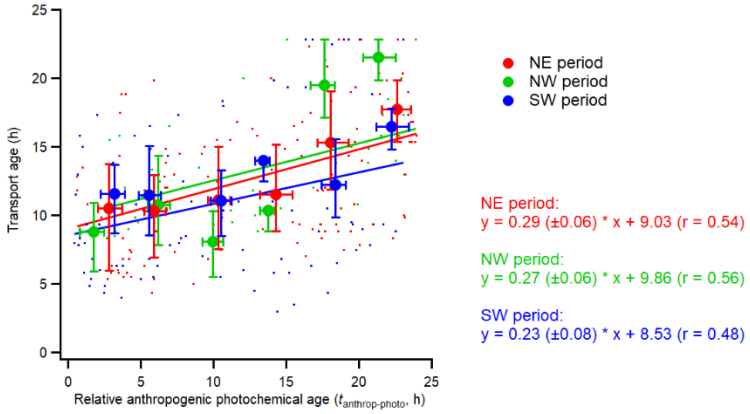

Figure S13 Comparison of the temporal trends in trajectory-based transport age and $t_{\mathrm{anthrop-photo}}$ derived from NO_x/NO_y ratios. The large markers represent the 4-hour binned averages, and the lower and upper whiskers indicate the 25th and 75th percentiles, respectively. The linear regression was performed using all data points within the same air-mass dominated period, and the fitting uncertainty represents ±1 standard deviation of the fit.

Figure S13 compares the trajectory-based transport age with $t_{\mathrm{anthrop-photo}}$ derived from NO_x/NO_y ratios for different air mass-dominated periods. The temporal evolution of $t_{\mathrm{anthrop-photo}}$ showed consistent temporal trends with those of the transport age, with moderate correlations (r = 0.48–0.56) across the different periods. While the correlations were moderate, this level of agreement is expected given the fundamentally different estimation approaches. Nevertheless, the comparable temporal trends between these independent indicators support the use of $t_{\mathrm{anthrop-photo}}$ as a proxy for relative photochemical aging during the campaign, as air masses with longer transport times generally undergo more extensive cumulative photochemical processing.

Reference

Ambrose, J. L., Haase, K., Russo, R. S., Zhou, Y., White, M. L., Frinak, E. K., Jordan, C., Mayne, H. R., Talbot, R., and Sive, B. C.: A comparison of GC-FID and PTR-MS toluene measurements in ambient air under conditions of enhanced monoterpene loading, Atmos. Meas. Tech., 3, 959–980, 10.5194/amt-3-959-2010, 2010.

Crippa, M., El Haddad, I., Slowik, J. G., DeCarlo, P. F., Mohr, C., Heringa, M. F., Chirico, R., Marchand, N., Sciare, J., Baltensperger, U., and Prévôt, A. S. H.: Identification of marine and continental aerosol sources in Paris using high resolution aerosol mass spectrometry, Journal of Geophysical Research: Atmospheres, 118, 1950–1963, https://doi.org/10.1002/jgrd.50151, 2013.

DeCarlo, P. F., Kimmel, J. R., Trimborn, A., Northway, M. J., Jayne, J. T., Aiken, A. C., Gonin, M., Fuhrer, K., Horvath, T., Docherty, K. S., Worsnop, D. R., and Jimenez, J. L.: Field-Deployable, High-Resolution, Time-of-Flight Aerosol Mass Spectrometer, Analytical Chemistry, 78, 8281–8289, 10.1021/ac061249n, 2006.

Jeon, S., Walker, M. J., Sueper, D. T., Day, D. A., Handschy, A. V., Jimenez, J. L., and Williams, B. J.: A searchable database and mass spectral comparison tool for the Aerosol Mass Spectrometer (AMS) and the Aerosol Chemical Speciation Monitor (ACSM), Atmos. Meas. Tech., 16, 6075–6095, 10.5194/amt-16-6075-2023, 2023.

Misztal, P. K., Hewitt, C. N., Wildt, J., Blande, J. D., Eller, A. S. D., Fares, S., Gentner, D. R., Gilman, J. B., Graus, M., Greenberg, J., Guenther, A. B., Hansel, A., Harley, P., Huang, M., Jardine, K., Karl, T., Kaser, L., Keutsch, F. N., Kiendler-Scharr, A., Kleist, E., Lerner, B. M., Li, T., Mak, J., Nölscher, A. C., Schnitzhofer, R., Sinha, V., Thornton, B., Warneke, C., Wegener, F., Werner, C., Williams, J., Worton, D. R., Yassaa, N., and Goldstein, A. H.: Atmospheric benzenoid emissions from plants rival those from fossil fuels, Scientific Reports, 5, 12064, 10.1038/srep12064, 2015.

Tani, A., Hayward, S., and Hewitt, C. N.: Measurement of monoterpenes and related compounds by proton transfer reaction-mass spectrometry (PTR-MS), International Journal of Mass Spectrometry, 223-224, 561–578, https://doi.org/10.1016/S1387-3806(02)00880-1, 2003.

White, M. L., Russo, R. S., Zhou, Y., Ambrose, J. L., Haase, K., Frinak, E. K., Varner, R. K., Wingenter, O. W., Mao, H., Talbot, R., and Sive, B. C.: Are biogenic emissions a significant source of summertime atmospheric toluene in the rural Northeastern United States?, Atmos. Chem. Phys., 9, 81–92, 10.5194/acp-9-81-2009, 2009.